Synthesis and Characterization of Core–Shell Magnetic Nanoparticles NiFe$_2$O$_4$@Au

Diana Saykova [1], Svetlana Saikova [1,2,*] , Yuri Mikhlin [2] , Marina Panteleeva [2], Ruslan Ivantsov [3] and Elena Belova [1]

[1] School of Non-Ferrous Metals and Material Science, Siberian Federal University, 660041 Krasnoyarsk, Russia; diana.saykova@mail.ru (D.S.); ebelova@sfu-kras.ru (E.B.)

[2] Institute of Chemistry and Chemical Technology, Federal Research Center "Krasnoyarsk Science Center of the Siberian Branch of the Russian Academy of Sciences", 660036 Krasnoyarsk, Russia; yumikh@icct.ru (Y.M.); vp414@mail.ru (M.P.)

[3] Kirensky Institute of Physics, Federal Research Center "Krasnoyarsk Science Center of the Siberian Branch of the Russian Academy of Sciences", Akademgorodok, 660036 Krasnoyarsk, Russia; ird@iph.krasn.ru

* Correspondence: ssai@mail.ru

check for updates

Abstract: In this study, NiFe$_2$O$_4$@Au core–shell nanoparticles were prepared by the direct reduction of gold on the magnetic surface using amino acid methionine as a reducer and a stabilizing agent simultaneously. The obtained nanoparticles after three steps of gold deposition had an average size of about 120 nm. The analysis of particles was performed by X-ray diffraction, transmission electron microscopy, X-ray photoelectron spectroscopy, and UV-Vis spectroscopy techniques. The results indicate successful synthesis of core–shell particles with the magnetic core, which consists of a few agglomerated nickel ferrite crystals with an average size 25.2 ± 2.0 nm, and the thick gold shell consists of fused Au^0 nanoparticles (NPs). Magnetic properties of the obtained nanoparticles were examined with magnetic circular dichroism. It was shown that the magnetic behavior of NiFe$_2$O$_4$@Au NPs is typical for superparamagnetic NPs and corresponds to that for NiFe$_2$O$_4$ NPs without a gold shell. The results indicate the successful synthesis of core–shell particles with the magnetic nickel ferrite core and thick gold shell, and open the potential for the application of the investigated hybrid nanoparticles in hyperthermia, targeted drug delivery, magnetic resonance imaging, or cell separation. The developed synthesis strategy can be extended to other metal ferrites and iron oxides.

Keywords: nickel ferrite nanoparticles; NiFe$_2$O$_4$@Au core–shell nanoparticles; synthesis; X-ray photoelectron spectroscopy; magnetic circular dichroism

1. Introduction

Reducing cancer mortality and increasing the success of cancer treatment begin with early diagnosis. Most early tumors do not produce any symptoms and are difficult to detect. Therefore, more sensitive materials that can be controlled from the outside and bound by cancer cells inside the body should be used for this purpose. Nanoparticles (NPs) with useful optical or magnetic properties are increasingly being used as a detective tool to spot tumors when they first develop [1,2]. It is possible to incorporate NPs into tumor tissue due to their small size. Then, an oscillating magnetic field can be applied so that magnetic nanoparticles interact with this field to generate heat and destroy cancer cells (the so-called hyperthermia). It is known that the heating of tissues up to 56 °C causes coagulation and carbonization of living cells. However, the temperature range from 40 °C to 46 °C can deactivate cancer cells without damaging healthy tissues. This process can be carried out under the influence of optical radiation (optical hyperthermia) or a high-frequency magnetic field (magnetic hyperthermia). A recent

review [3] considers, in detail, different aspects of thermal therapies of cancer diseases. The application of magnetic nanopowders in medicine is possible due to their ability to heat up under the influence of a variable magnetic field because of the different types of thermal losses (eddy currents, magnetization reversal losses, and mechanical rotation of nanoparticles). This method is also referred to as magnetic fluid hyperthermia [4].

Nickel ferrite is an important magnetic material due to its high magnetic permeability at high frequencies, high electrical conductivity, mechanical strength, and its low cost. Nickel ferrite is widely used in electrical devices, as a contrasting agent in magnetic resonance imaging, as an anode in lithium-ion batteries, and as a catalyst for the halogenation of aromatic compounds [5]. In addition, the material is easily heated under the action of an external magnetic field and can be used for cancer hyperthermia. However, it has been shown [6] that $NiFe_2O_4$ nanoparticles induce cytotoxicity and, like other magnetic nanoparticles, tend to aggregate under physiological conditions. In order to avoid these complications, the covering of nickel ferrite nanoparticles with an inert shell is used. The shell would ensure stability of NPs and provide ease of functionalization. Gold is commonly used for the synthesis of hybrid nanoparticles [7–10], and SiO_2 [11] or Ag [12] is sometimes also applied. The combination of the components of different chemical nature in such hybrid nanoparticles leads to the formation of a material with improved characteristics compared to its individual components. The components enhance useful properties and eliminate the disadvantages of each material. Fe_3O_4 [7,11,13], Fe [14], $CoFe_2O_4$ [15,16], and $NiFe_2O_4$ [12] are most often used as the cores of hybrid magnetic particles.

The literature shows two main approaches to attaching gold to magnetic particles. According to the first approach, gold seeds prepared separately are fixed on the surface of the magnetic core by co-precipitation after (or with) the formation of a polymer shell, which is used to stabilize the particles. Special molecules, the so-called "anchors", are used to attach gold to the surface of the core. Such molecules are dopamine hydrochloride [7], 3-amino-propyltrimethoxysilane, and cysteamine in the presence of carbonyldiimidazole. The second approach, used in [8–10,13–17], involves the straightforward growth of Au NPs directly onto the magnetic core without using gold seeds. A variety of reducing agents can be used to reduce $[AuCl_4]^-$ to gold powder including 1,2-hexadecandiol [13], ascorbic acid [10,16], methionine [15], sodium citrate and hydroxylamine chloride [10,18–20], and sodium borohydride [9]. Moreover, the process is conducted both in aqueous and non-aqueous [8,9] or mixed [13,18] environments. In some cases, the surface of the nuclei is additionally treated with tetramethylammonium [19], functionalized with amino [9] or OH-groups [8], or covered with a shell of SiO_2 [11].

While the literature on the synthesis of hybrid nanoparticles for biomedical applications is vast, little show the formation of a continuous gold shell [21]. In many studies, particles decorated with gold seeds are formed [11,15,16]. These NPs cannot be grown to a continuous shell. In addition, the reproducibility of experimental results remains a major problem.

To the best of our knowledge, only a few studies have been undertaken where nickel ferrite was used as magnetic nuclei. $NiFe_2O_4$ is known to belong to the family of soft ferrite materials with high magnetic permeability [22,23], low core losses, high saturation magnetization, dielectric resistivity, and low Curie temperature [24,25]. Soft magnetic materials are more convenient and desirable for fine temperature control to achieve the temperature range required for magnetic fluid hyperthermia (40–46 °C) [4]. Thus, the aim of the study was to provide a reliable synthetic strategy to obtain hybrid nanoparticles based on nickel ferrite nanoparticles with a continuous gold shell and to characterize the products by X-ray diffraction (XRD), X-ray photoelectron spectroscopy (XPS), and transmission electron microscopy (TEM).

2. Materials and Methods

2.1. Chemicals

Nickel nitrate $Ni(NO_3)_2 \cdot 7H_2O$, iron nitrate $Fe(NO_3)_3 \cdot 9H_2O$, L-methionine, and other chemicals were of analytical grade, purchased from Sigma-Aldrich, and used as received.

2.2. Synthesis of Nickel Ferrite Nanoparticles

In this study, Ni ferrite nanoparticles were synthesized by the co-precipitation method. In a typical procedure, 10 mL $Ni(NO_3)_2$ (0.4 mol/L) was mixed with 10 mL $Fe(NO_3)_3$ (0.8 mol/L), 0.5 mL tartaric acid (0.1 mol/L), and 0.0728 g cetrimonium bromide (CTAB). The pH of the solution was dropped to 10 by adding 1 mol/L NaOH for 5 min. The mixture was stirred (1000 rpm) for 2 h at a temperature of 25 °C using a magnetic stirrer. The precipitate was centrifuged, washed with distilled water, dried in air at 80 °C for 2 h, and finally annealed in a muffle furnace for 3 h at 650 °C.

2.3. Gold Shell Formation

Hybrid $NiFe_2O_4$@Au nanoparticles were fabricated by methionine-directed gold deposition from $HAuCl_4$ solution according to the modified technique described in [15]. Shortly, 25 mg of nickel ferrite nanoparticles was dispersed in 20 mL of aqueous 0.03 mol/L L-methionine by ultrasonic agitation (ultrasonic bath "Sapphire") for 30 min. Then, 1 mL chlorauric acid (0.1 mol/L) was added to the mixture; the pH was adjusted to 10 by addition of 1 mol/L NaOH. The deposition process was conducted at 37 °C for 4 h under stirring (800 rpm). The products were centrifuged, washed with distilled water, and redispersed in ethanol for further investigations. The procedure of gold deposition was repeated 2 times under the same conditions.

2.4. Characterization/Analysis

UV-vis absorption spectra were collected in a glass cell with an optical path of 1 cm employing a Specol spectrometer (Carl Zeiss, Jena, Germany). X-ray photoelectron spectroscopy studies were performed using a hydrosol dried with highly oriented pyrolytic graphite (HOPG) and gently rinsed with water. The spectra were acquired using a Shimadzu XRD-600 diffractometer (Shimadzu Corporation, Kyoto, Japan) employing monochromatic Cu Kα radiation. The analyzer pass energy was 10 eV for high-resolution scans and 20 eV for survey spectra. An electron flood gun was applied to eliminate inhomogeneous electrostatic charging of the samples; the C 1s peak at 284.45 eV from HOPG was used as a reference. The high-resolution spectra were fitted after subtraction of Shirley-type background with Gaussian–Lorentzian peak profiles, using CasaXPS software (version 2.3.16, Casa Software, Teignmouth, UK). Transmission electron microscopy was carried out using an HT-7700 instrument (Hitachi Corporation, Hitachi, Japan) operating at an accelerating voltage of 100 kV. A nickel ferrite particle size distribution histogram has been obtained from more than three hundred particles. Magnetic properties of the obtained nanoparticles were examined with magnetic circular dichroism (MCD)—one of the most informative magneto-optical effects. By being linear in magnetization, the MCD allows one to trace the behavior of the magnetic moment of the sample in an external magnetic field and at various external influences. On the other hand, the study of the spectral dependences of MCD provides information on electronic excitations in a substance under the influence of optical radiation and allows one to obtain the structure of excited levels characteristic of each substance. To carry out the MCD measurements, transparent composite plates containing the $NiFe_2O_4$ NPs were prepared according to the method described in [26]. Measurements were carried out in the spectral range of 1.3–3.9 eV in a magnetic field of 1.3 T at the temperature of 300 K also analogously to [26]. The measurement accuracy was about 10^{-4}, and the spectral resolution was 20–50 cm^{-1} depending on the wavelength.

3. Results

3.1. Fabrication and Characterization of Nickel Ferrite Nanoparticles

In this study, Ni ferrite nanoparticles were synthesized by tartaric acid and the cetrimonium bromide-assisted co-precipitation reaction of Ni(II) and Fe(III) salts (pH 10, NaOH) at 25 °C for 2 h followed by several rinsing and centrifugation procedures, as reported earlier [27,28]. The products annealed for 3 h at 650 °C were investigated by the methods of X-ray powder diffraction, X-ray photoelectron spectroscopy, and transmission electron microscopy. The crystalline nature of nickel ferrite NPs was verified by X-ray diffraction investigations. The representative XRD pattern of the NPs is shown in Figure 1a. The position and relative intensity of all diffraction peaks (18.44°; 30.33°; 35.73°; 37.37°; 43.43°; 53.89°; 57.45°) match well with the standard $NiFe_2O_4$ diffraction data; no other secondary phase is observed. The average nanoparticle crystallite size was determined from the peak broadening for the four most intensive powder XRD peaks (30.33°; 35.73°; 43.43°; 57.45°) using the Scherrer equation (Equation (1)), and it was 24.8 nm.

$$D = b \cdot \lambda / FHWM \cdot \cos\theta, \tag{1}$$

where FWHM is the full-width at half-maximum intensity of the peak, 2θ is the scattering angle in radians, λ is the wavelength (1.5406 Å), b is a constant that is a function of the crystallite geometry, normally taking a value between 0.89 and 0.94, and D is the average size of the crystallites.
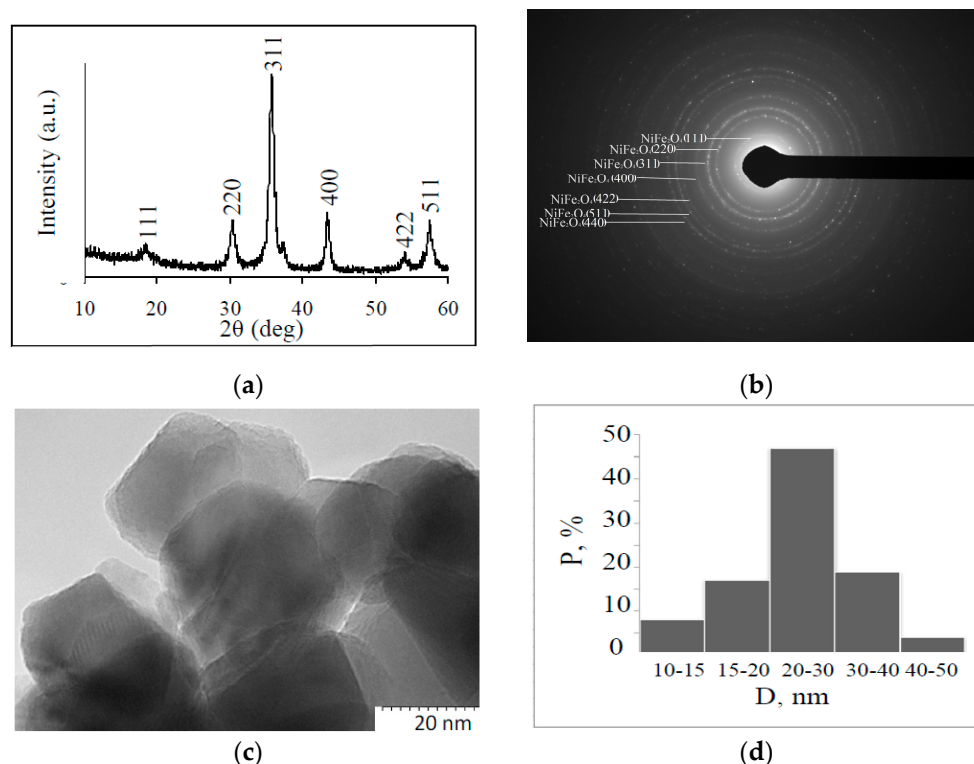
Figure 1. (**a**) XRD pattern, (**b**) electron diffraction pattern, (**c**) TEM image, (**d**) size distribution histogram of nickel ferrite particles synthesized by co-precipitation in the solution containing $0.2Ni(NO_3)_2$ + $0.4Fe(NO_3)_3$ + 0.01 cetrimonium bromide (CTAB) + 2×10^{-3} mol/L tartaric acid + 1 mol/L NaOH up to pH = 10 at 25 °C for 5 min.

Figure 1 shows the TEM image of $NiFe_2O_4$ NPs (Figure 1c) and their size distribution histogram (Figure 1d). TEM analysis demonstrates that the particles are faceted in shape and their size is 20–30 nm.

This was found to be in good agreement with the crystallite size (15 nm) obtained from the powder XRD data. As a result, we produce the material suitable for hybrid nanoparticles synthesis.

3.2. Fabrication and Characterization of NiFe$_2$O$_4$@Au

The literature demonstrates two main approaches to the synthesis of hybrid nanoparticles based on magnetite or ferrites and noble metals. The first is the adsorption of gold seeds on the surface of magnetic nanoparticles, the second is a direct gold reduction from HAuCl$_4$ solution on the NPs surface. We used the second approach adapting the technique from [15]. The deposition process was conducted using 2-amino-4-(methylthio) butanoic acid (methionine) as a reducer of gold species and a stabilizing agent at 37 °C for 4 h under vigorous stirring. The procedure of gold deposition (coating) was repeated two times under the same conditions.

Among the 20 natural amino acids that are incorporated into proteins, only the tyrosine, tryptophan, histidine, cysteine, and methionine are oxidized at carbon electrodes and can be used for gold species reduction. However, methionine, unlike the other gold-reducing amino acids, does not form separate gold crystals in the bulk of the solution [15]. In addition, methionine plays the key role as the antioxidant, which defends the structure and stability of proteins [29–33]. Methionine is a sulfur-containing amino acid. The chemical linkage of the sulfur in methionine is a thiol ether. Combining several active centers in the methionine molecule (the sulfur atom, an amine group, and a carboxyl group) results in using it as an anchor between the NiFe$_2$O$_4$ surface and gold. First, methionine is adsorbed on the nickel ferrite NPs surface via NH$_2$-groups. Then, methionine reduces tetrachloroauric (III) acid to Au (I), which disproportions to form Au (III) species and metallic gold. Gold attaches to the NPs surface through a thiol ether atom of methionine.

In order to coat particles, nickel ferrite powder was mixed with aqueous solutions of methionine and gold (HAuCl$_4$) (1:6:1 molar ratio, respectively) and stirred for 4 h at 37 °C. The hybrid particles were separated by magnetic separation, washed, and dried.

The obtained particles redispersed in ethanol (sample 1) and the solution remaining after separation of the magnetic particles (sample 2) were studied by a spectrophotometer in the wavelength range of 400–1000 nm. Figure 2 shows that both samples have the absorption maximum of gold nanoparticles [30]: Sample 1 at 560 nm (Figure 2a), sample 2 at 580 nm. However, after the separation of nanoparticles, the solution contains a very small amount of gold. Its optical density is much lower than the optical density of the hydrosol of the obtained particles. This indicates that the reduction of gold occurs not in the volume of the solution but on the surface of the ferrite.

(a) **(b)**
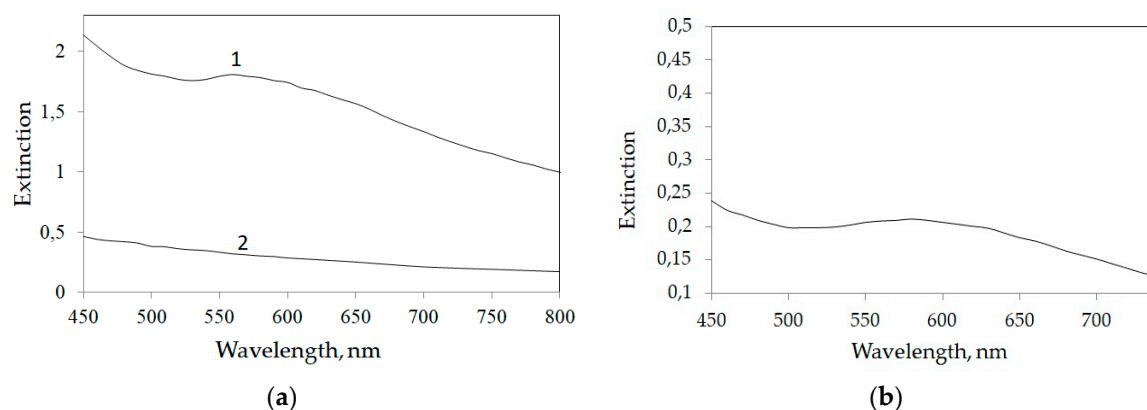
Figure 2. Optical absorption spectra of NiFe$_2$O$_4$ nanoparticles (**a**) before (2) and after (1) gold deposition from the alkaline (pH = 10) solution containing 0.1 mol/L HAuCl$_4$ and 0.03 mol/L methionine at 37 °C for 4 h, and spectra of solution (**b**) remaining after NiFe$_2$O$_4$@Au nanoparticles (NPs) magnetic separation.

The obtained hybrid particles were examined by transmission electron microscopy. After a single coating (Figure 3a), the surface of magnetic particles is inlaid with gold seeds (2–3 nm), i.e., gold is not epitaxially deposited on the surface of the ferrite, and the coating is patchy [31]. The electron diffraction spectrum of NiFe$_2$O$_4$@Au NPs after a single coating (Figure 3b) contains diffraction rings corresponding to both nickel ferrite and gold. A thin layer around the particles in the TEM image in Figure 3a is noticeable. From our point of view, the layer is the product of methionine oxidation and it allows for the attachment of the Au colloid to the nanocrystal surface. The adsorbed seeds are densely located, which allows us to expect their fusion during their growth. In order to grow the gold shell, the coating was repeated two more times, replacing the initial ferrite with inlaid magnetic cores.
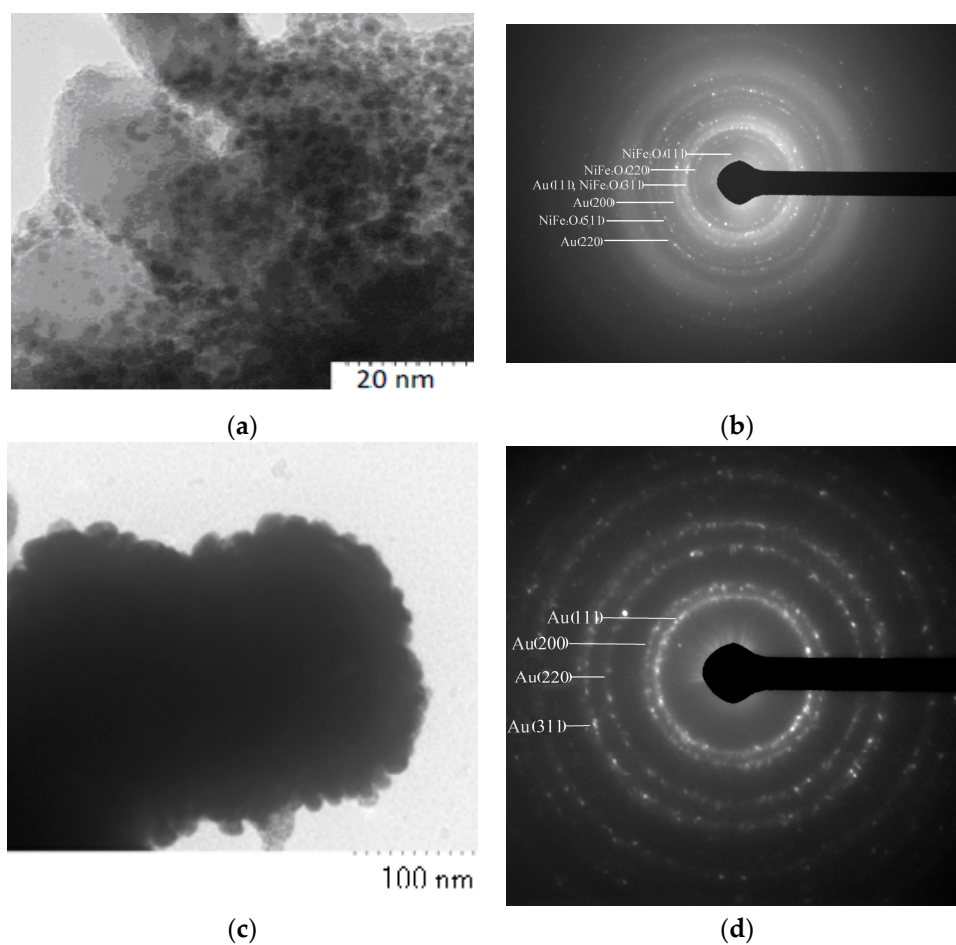
Figure 3. TEM images (**a**,**c**) and electron diffraction patterns (**b**,**d**) of hybrid NiFe$_2$O$_4$@Au NPs after methionine-directed gold deposition under conditions in Figure 2: (**a**,**b**) Single-stage coating; (**c**,**d**) three-stage coating.

According to the TEM data (Figure 3c), an increase in the number of coating stages leads to the growth of seeds. We observe the formation of a continuous gold shell on the surface of the several agglomerated nickel ferrite crystals. The NiFe$_2$O$_4$@Au hybrid particles diameter increases from 20–30 to 120 nm, which indicates that the gold coating is most likely not a single layer. In addition, the gold coating has significant thickness; diffraction rings of gold are only observed in the electron microdiffraction pattern (Figure 3d). Gold is strongly fixed on the NPs and not detached from the magnetic core under the influence of a magnetic field and during post-synthetic processing (washing, redispersion, ultrasound treatment).

However, there are reflexes of nickel ferrite of 18.44°; 30.33°; 35.73°; 43.43°; 53.89°; 57.45°; and 63.1°, and gold 38.1°; 44.28°; and 64.42°, on the X-ray pattern of the products (Figure 4, curve 2). With an increase in the number of coating stages from two (curve 1, Figure 4) to three (curve 2, Figure 4), the intensity of the gold maximum increases and the relative Au^0 concentration increases from 15 to 36%. This indicates a denser coating of the magnetic nuclei. The difference between the TEM and XRD results is explained by the fact that these methods have different resolutions in depth.
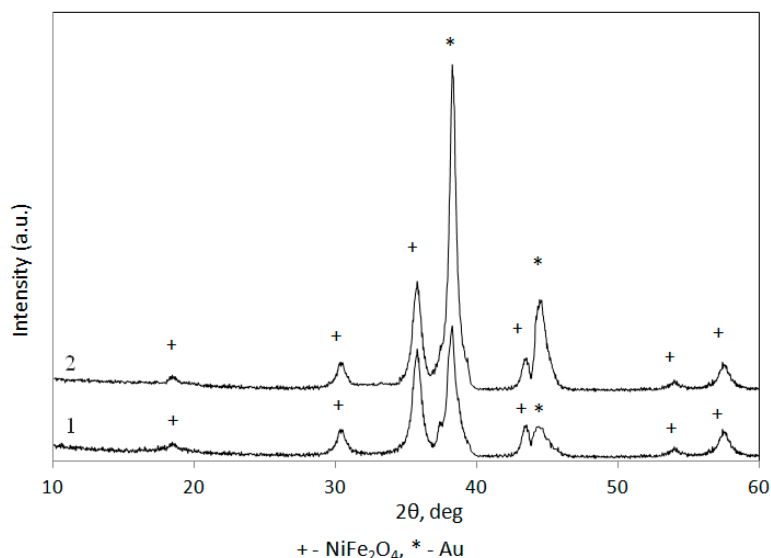
Figure 4. XRD patterns of $NiFe_2O_4$@Au NPs after gold deposition under conditions in Figure 2: (curve 1) Two-stage coating and (curve 2) three-stage coating.

We calculate the average nanoparticle crystallite size using the Scherrer equation from XRD patterns of $NiFe_2O_4$@Au NPs after two-stage and three-stage gold deposition (Figure 4). Moreover, the XRD peaks of the $NiFe_2O_4$ phase (30.33°; 35.73°; 57.45°) and XRD peak of the Au^0 phase (38.1°) were used for the calculation separately. The average nanoparticle crystalline size determined for the peaks of the $NiFe_2O_4$ phase for both samples (after two-stage and three-stage coating) was 25.2 ± 2.0 nm, which corresponds to the $NiFe_2O_4$ particle size before coating. At the same time, the NP sizes determined for the peaks of the gold phase was 23.5 nm (two-stage coating) and 25.5 nm (three-stage coating). These findings confirm that the gold shell covers several nickel ferrite crystals, whose size does not change in the gold deposition process. However, small gold seeds obtained in the first coating step significantly increase in size during the second step and form the continuous gold shell during the third stage.

X-ray photoelectron spectroscopy was applied to study the surface composition and chemical state of elements in the hybrid nanoparticles $NiFe_2O_4$@Au (Figure 5). The survey spectrum of gold-coated nickel ferrite nanoparticles (Figure 5a) contains peaks of Au 4f, S 2p, O 1s, and C 1s, while the lines of Fe 2p (Figure 5b) and Ni are almost absent, confirming the formation of a continuous gold shell (Figure 3). The peak of N 1s was not observed either, while the Au/S atomic ratio was 3.3 (Table 1). This indicates a lack of methionine or methionine sulfoxide CH_3-$S(O)CH_2CH_2C(NH_2)COOH$ that is believed to be the product of methionine oxidation by Au^{3+} [32].
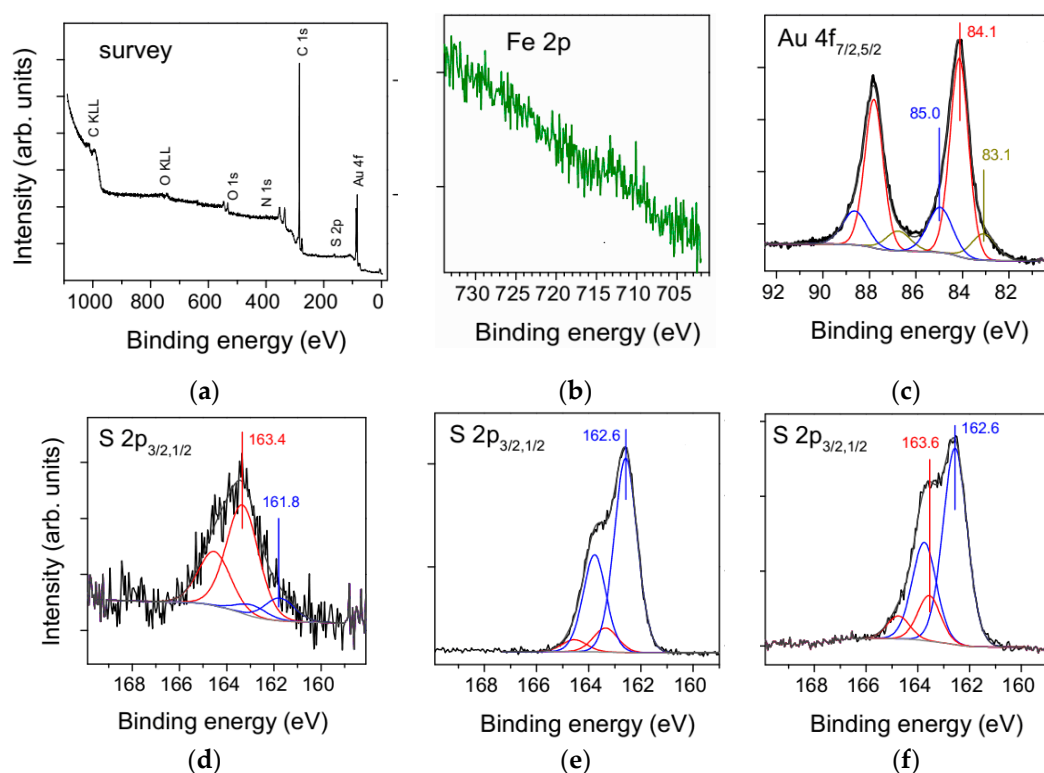
Figure 5. XPS spectra of the Au 4f, Fe 2p, S 2p, and O 1s photoelectron, respectively (**a**–**d**), for the gold-coated nickel ferrite nanoparticles synthesized under conditions in Figure 2 (three-stage coating), S2p spectra from the methionine (**e**) and the product of its interaction with aqueous $AuCl_4^-$ complex (**f**).

Table 1. Concentrations of main elements derived from XPS analysis.

Sample	Relative Concentrations (At. %)		
	S	N	Au
Methionine	3.9	3.7	-
Methionine + HAuCl$_4$	6.8	4.9	0.6
NiFe$_2$O$_4$@Au	14.0	0	47.0

We compared photoelectron S2p spectra from the nanocomposite with those of methionine and the product of its interaction with aqueous $AuCl_4^-$ complex (Figure 5d–f). The spectrum of methionine (Figure 5e) shows a predominant doublet with a binding energy S $2p_{3/2}$ of 162.6, which can be assigned to the thioether group C-S-C [34,35]. After the reaction with $AuCl_4^-$ at the molar ratio of methionine to Au of 10, the major doublet does not change their position, due to the large excess of methionine (Figure 5f), while an additional minor doublet with the binding energy S2p$_{3/2}$ of 163.5 eV, which is attributable to a product of methionine oxidation, increases. At the same time, the atomic ratio of sulfur/nitrogen (Table 1) grows from about 1 to 1.4. This may be explained in terms of the dimerization of methionine with the formation of two-center three-electron (2c–3e) S–S bonds [36] or, most likely, the formation of gold sulfide. The lines with S2p$_{3/2}$ binding energies of ~163.5, 162.5, and 161.6 eV, which are typically assigned to polysulfide, disulfide, and monosulfide species, respectively, were observed both for sulfur chemisorbed on gold and gold (I) sulfide that tends to decompose to Au^0 nanoparticles capped with sulfur [37,38]. This means that the interpretation of photoelectron spectra of gold sulfide still remains unclear.

The S2p spectrum acquired from hybrid nanoparticles NiFe$_2$O$_4$@Au (Figure 5d) is better fitted using a high-intensity doublet with the S2p$_{3/2}$ peak at 163.3 eV and a smaller one at 161.8 eV. These

signals should be attributed mainly to gold sulfide, and possibly minor chemisorbed sulfur Fe and Ni sulfides, as nitrogen, and so methionine is absent.

The Au $4f_{7/2,5/2}$ spectrum of gold deposited on nickel ferrite (Figure 5c) differs from that of elemental gold and can be fitted by three components. The major doublet with the binding energy of the Au $4f_{7/2}$ peak of 84.1 eV corresponds to metallic Au; the component at 85.0 eV is due to Au^+ species probably in gold sulfide, in agreement with the S 2p spectra and the relative element ratio (Table 1), and the third doublet has an Au $4f_{7/2}$ binding energy as low as 83.1 eV. Such a significant negative shift is likely associated with electron transfer from the support to the Au particle [39,40].

It has been reported [41] that an excess of oxygen atoms is observed on the surface of oxides as a result of oxygen vacancies in the bulk of the oxide lattice. The gold atoms are adsorbed on these sites and the charge transfers from electron-rich O atoms to Au atoms. As shown in [42], the oxygen vacancies exist in most oxides and they are more typical for nickel ferrite.

Even though lots of research has been done, the chemical mechanism of methionine oxidation by $[AuCl_4]^-$ ions is still not understood. According to the literature data [32,33], the reaction mechanism takes place in a few steps. The first step is a very fast coordination of methionine (Met) to the Au(III) ion. Met acts as a bidentate S- and N-donor ligand and displaces the chloride anion in $[AuCl_4]^-$, forming intermediate complex $[AuCl_2(HMet)]^{2+}$ (in acidic solutions) or $[AuCl_2(Met)]^+$ (in alkaline solutions). Several authors maintain that the Au(III) ion coordinates only to the thioether sulfur and forms $[AuCl_3(HMet)]^+$. At the second stage, the reduction of Met takes place: The intermediate product reacts with the second methionine molecule to generate Met sulfoxide as the product of the redox process. As a result, a $[AuCl_2]^-$ complex is formed. In addition, $[AuCl_2]^-$ finally disproportions very fast in the aqueous solution, forming $[AuCl_4]^-$ and metallic gold:

$$3[AuCl_2]^- = 2Au^0 + [AuCl_4]^- + 2Cl^-. \tag{2}$$

Figure 6 shows the MCD spectra of samples containing $NiFe_2O_4$ and $NiFe_2O_4@Au$ NPs after three-stage gold deposition (empty and filled circles, correspondingly).
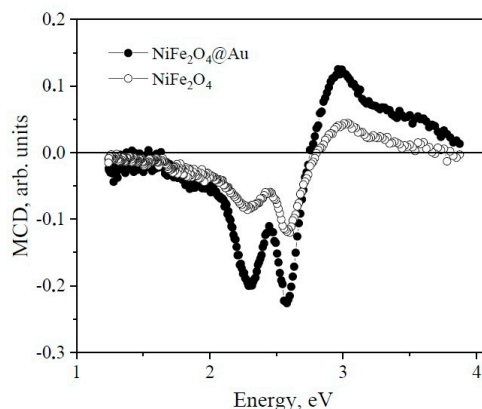
Figure 6. Room-temperature magnetic circular dichroism (MCD) spectra of $NiFe_2O_4$ and $NiFe_2O_4@Au$ (three-stage coating) NPs recorded in magnetic field of 10 kOe.

The spectra of both samples demonstrate the same shape: Strong positive maximum in the higher-energy part of the spectrum and two close negative maxima are the most prominent features of the spectra. Coincidence of the two curves evidences that the observed MCD is due to the magnetic NPs or magnetic core only. The gold shell can cause an increase in the MCD signal, but this question needs further investigation. As there are no data in the literature on the MCD spectra of stoichiometric $NiFe_2O_4$ (possibly because of the difficulties in the measurements in the transmitted light), we can compare them with the spectra of the off-diagonal components of the dielectric tensor, which were determined in several works based on the Kerr effect measurements in the reflected light.

Such a comparison is fully justified by the fact that the MCD, like the Kerr effect, is determined by these components. In particular, the expression for MCD has the form [43]:

$$\theta = \frac{4\pi}{\lambda}\left\{\frac{n}{k^2+n^2}\varepsilon'_{xy} - \frac{k}{k^2+n^2}\dot{\varepsilon}_{xy}\right\} \tag{3}$$

where $\dot{\varepsilon}_{xy}$ and ε'_{xy} are the real and imaginary parts of the off-diagonal component of the dielectric tensor ε, respectively; n and k are the refractive index and absorption coefficient, respectively; and λ is the light wavelength. In the considered spectral region, k is significantly lower compared to n, and θ depends mainly on the first term in brackets. The second term, as well the k and n dependences on the wavelength, can cause some deviations in the MCD spectrum from the spectrum of ε'_{xy}. Comparison of the MCD spectra shown in Figure 6 with the ε'_{xy} spectrum for the epitaxial NiFe$_2$O$_4$ thin film presented in [44] demonstrates coincidence of all their main features, that is, the MCD spectrum observed in the fabricated NPs is typical for the nickel ferrite. At that, the negative MCD maximum centered near 2.55 eV and positive one centered near 3 eV can be associated, according to [44], with the charge transfer electron transitions inter-sublattice (Fe^{3+})t$_2$→[Fe^{3+}]t$_{2g}$ and inter-valence [Ni^{2+}]t$_{2g}$→[Fe^{3+}]t$_{2g}$, correspondingly.

The MCD dependence on magnetic field for NiFe$_2$O$_4$@Au NPs shown in Figure 7 is typical for superparamagnetic NPs (NiFe$_2$O$_4$ NPs without gold shell show similar behavior). A similar dependence was observed recently in [45] for NiFe$_2$O$_4$ NPs of 9.2 nm in diameter synthesized by forced hydrolysis. Thus, the magnetic behavior of NiFe$_2$O$_4$@Au NPs corresponds to that presented in the literature for NiFe$_2$O$_4$ NPs.
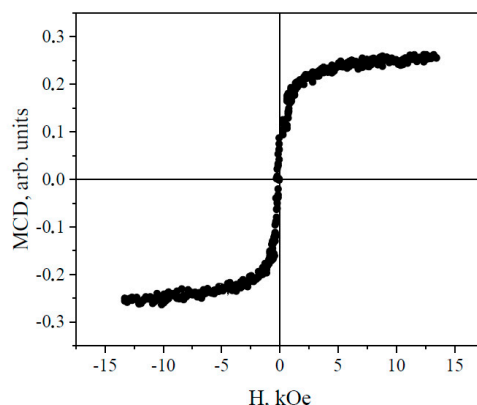
Figure 7. The MCD signal dependence on magnetic field for NiFe$_2$O$_4$@Au NPs (three-stage coating) recorded at the energy of 2.6 eV.

4. Conclusions

This study describes a successful synthesis of core–shell nanoparticles with a magnetic nickel ferrite core and a gold shell using amino acid methionine as a reducer and a stabilizing agent simultaneously. The phase composition of the nanoparticles corresponds to the structure of NiFe$_2$O$_4$ and gold with characteristic reflexes: <30.33>; <35.73>; <43.43>, and <38.1>; <44.28>; <64.42>. The obtained nanoparticles consist of a magnetic core, which includes a few agglomerated nickel ferrite crystals with the average size of 25.2 ± 2.0 nm, and the thick gold shell consists of fused Au^0 NPs. The survey spectrum (XPS) of gold-coated nickel ferrite nanoparticles contains peaks of Au 4f, S 2p, O 1s, and C 1s, while the lines of Fe 2p and Ni are almost absent, confirming the formation of a continuous gold shell. The TEM and XRD data show an increase in the number of coating stages, which leads to the growth of seeds on a thick shell. The particle diameter increases from 20–30 nm (for NiFe$_2$O$_4$ NPs) to 120 nm (for hybrid particles). The formation of core–shell NiFe$_2$O$_4$@Au particles is proved by TEM, XRD, and XPS analysis. The magnetic properties of the obtained nanoparticles

of magnetic circular dichroism (MCD) are due to the magnetic core only. The magnetic behavior of NiFe$_2$O$_4$@Au is typical for superparamagnetic NPs and corresponds to that for NiFe$_2$O$_4$ NPs without a gold shell. The continuous shell of the synthesized particles demonstrates properties that can be used for biomedical applications in cancer diagnosis and treatment. The developed strategy can be extended to other metal ferrites and iron oxides.

References

1. Yang, D.; Deng, F.; Liu, D.; He, B.; He, B.; Tang, X.; Zhang, Q. The appliances and prospects of aurum nanomaterials in biodiagnostics, imaging, drug delivery and combination therapy. *J. Pharm. Sci.* **2018**, *13*, 143–153. [CrossRef]

2. Long, F.; Li, W.; Chen, W.; Liu, D.; Chen, Y.; Zhou, R.; Li, P. Amperometric Biosensor Based on Cu$_2$O@Au Nanocomposites for the Detection of Galectin-1 via Lactose-Galectin Interactions. *Nanotechnology* **2019**, *30*, 485706. [CrossRef]

3. Jaque, D.; Martinez Maestro, L.; del Rosal, B.; Haro-Gonzalez, P.; Benayas, A.; Plaza, J.L.; Martin Rodriguez, E.; Garcia Sole, J. Nanoparticles for photothermal therapies. *Nanoscale* **2014**, *6*, 9494–9530. [CrossRef] [PubMed]

4. Balanov, V.A.; Kiseleva, A.P.; Krivoshapkina, E.F.; Kashtanov, E.A.; Gimaev, R.R.; Zverev, V.I.; Krivoshapkin, P.V. Synthesis of (Mn$_{(1-x)}$Zn$_x$)Fe$_2$O$_4$ nanoparticles for magnetocaloric applications. *J. Sol-Gel Sci. Technol.* **2020**, 1–6. [CrossRef]

5. Maaz, K.; Karim, S.; Mumtaz, A.; Hasanain, S.K.; Liu, J.; Duan, J.L. Synthesis and magnetic characterization of nickel ferrite nanoparticles prepared by co-precipitation route. *J. Magn. Magn. Mater.* **2009**, *321*, 1838–1842. [CrossRef]

6. Ahamed, M.; Akhtar, M.J.; Alhadlaq, H.A.; Khan, M.A.M.; Alrokayan, S.A. Comparative cytotoxic response of nickel ferrite nanoparticles in human liver HepG2 and breast MFC-7 cancer cells. *Chemosphere* **2015**, *135*, 278–288. [CrossRef]

7. An, P.; Zuo, F.; Li, X.; Wu, Y.; Zhang, J.; Zheng, Z.; Ding, X.; Peng, Y. A bio-inspired polydopamine approach to preparation of gold-coated Fe$_3$O$_4$ core-shell nanoparticles: Synthesis, characterization and mechanism. *NANO* **2013**, *8*, 1350061. [CrossRef]

8. Xu, C.; Wang, B.; Sun, S. Dumbbell-like functional Au−Fe$_3$O$_4$ Nanoparticles for Target-Specific Platin Delivery. *J. Am. Chem. Soc.* **2009**, *131*, 4216–4217. [CrossRef]

9. Billen, A.; de Cattelle, A.; Jochum, J.K.; Van Bael, M.J.; Billen, J.; Seo, J.W.; Brullot, W.; Koeckelberghs, G.; Verbiest, T. Novel synthesis of superparamagnetic plasmonic core-shell iron oxide-gold nanoparticles. *Physica B* **2019**, *560*, 85–90. [CrossRef]

10. Li, Y.; Liu, J.; Zhong, Y.; Zhang, J.; Wang, Z.; Wang, L.; An, Y.; Lin, M.; Gao, Z.; Zhang, D. Biocompatibility of Fe$_3$O$_4$@Au composite magnetic nanoparticles in vitro and in vivo. *Int. J. Nanomed.* **2011**, *6*, 2805–2819. [CrossRef]

11. Stoeva, S.I.; Huo, F.; Lee, J.-S.; Mirkin, C.A. Three-Layer Composite Magnetic Nanoparticle Probes for DNA. *J. Am. Chem. Soc.* **2005**, *127*, 15362–15363. [CrossRef]

12. Blanco-Esqueda, I.G.; Ortega-Zarzosa, G.; Martínez, J.R.; Guerrero, A.L. Preparation and Characterization of Nickel Ferrite-SiO$_2$/Ag Core/Shell Nanocomposites. *Adv. Mater. Sci. Eng.* **2015**, *2015*, 678739. [CrossRef]

13. Smith, M.K.; Mc Keague, M.; Rosa, C.D. Synthesis, transfer, and characterization of core-shell gold-coated magnetic nanoparticles. *MethodsX* **2019**, *6*, 333–354. [CrossRef] [PubMed]

14. Ahmandi, N.; Poursalehi, R.; Kirilyuk, A.; Moravvej-Farshi, M.K. Effect of gold plasmonic shell on nonlinear optical characteristics and structure of iron based nanoparticles. *Appl. Surf. Sci.* **2019**, *479*, 114–118. [CrossRef]

15. Mikalauskaite, A.; Kondrotas, R.; Niaura, G.; Jagminas, A. Gold-Coated Cobalt Ferrite Nanoparticles via Methionine-Induced Reduction. *J. Phys. Chem.* **2015**, *119*, 17398–17407. [CrossRef]

16. Jagminas, A.; Mažeika, K.; Kondrotas, R.; Kurtinaitienė, M.; Jagminienė, A.; Mikalauskaite, A. Functionalization of cobalt ferrite nanoparticles by a vitamin C-assisted covering with gold. *Nanomater. Nanotechno.* **2014**, *4*, 4–9. [CrossRef]

17. Lu, Z.-R.; Kopeckova, P.; Wu, Z.; Kopecek, J. Synthesis of semitelechelic poly[N-(2-hydroxypropyl)metacrylamide] by radical polymerization in the presence of alkyl mercaptans. *Macromol. Chem. Phys.* **1999**, *200*, 2022–2030. [CrossRef]

18. Silvestri, A.; Mondini, S.; Marelli, M.; Pifferi, V.; Falciola, L.; Ponti, A.; Polito, L. Synthesis of Water Dispersible and Catalytically Active Gold-Decorated Cobalt Ferrite Nanoparticles. *Langmuir* **2016**, *32*, 7117–7126. [CrossRef]

19. Zeng, J.; Gong, M.; Wang, D.; Li, M.; Xu, W.; Li, Z.; Li, S.; Zhang, D.; Yan, Z.; Yin, Y. Direct synthesis of water-dispersible magnetic/plasmonic hetero-nanostructures for multi-modality biomedical imaging. *Nano Lett.* **2019**, *19*, 3011–3019. [CrossRef]

20. Kumal, R.R.; Abu-Laban, M.; Hamal, P.; Kruger, B.; Smith, H.T.; Hayes, D.J.; Haber, L.H. Near-infrared photothermal release of SiRNA from the surface of colloidal gold-silver-gold core-shell-shell nanoparticles studied with second-harmonic generation. *J. Phys. Chem.* **2018**, *122*, 19699–19704. [CrossRef]

21. Tschulik, K.; Ngamchuea, K.; Ziegler, C.; Beier, M.G.; Damm, C.; Eychmueller, A.; Compton, R.G. Core–Shell Nanoparticles: Characterizing Multifunctional Materials beyond Imaging—Distinguishing and Quantifying Perfect and Broken Shells. *Adv. Funct. Mater.* **2015**, *25*, 5149–5158. [CrossRef]

22. Chauhan, L.; Shukla, A.K.; Sreenivas, K. Dielectric and magnetic properties of Nickel ferrite ceramics using crystalline powders derived from DL alanine fuel in sol–gel auto-combustion. *Ceram. Int.* **2015**, *41*, 8341–8351. [CrossRef]

23. Nabiyouni, G.; Jafari Fesharaki, M.; Mozafari, M.; Amighian, J. Characterization and Magnetic Properties of Nickel Ferrite Nanoparticles Prepared by Ball Milling Technique. *Chin. Phys. Lett.* **2010**, *27*, 126401. [CrossRef]

24. He, X.; Zhong, W.; Au, C.-T.; Du, Y. Size dependence of the magnetic properties of Ni nanoparticles prepared by thermal decomposition method. *Nanoscale Res. Lett.* **2013**, *8*, 446. [CrossRef] [PubMed]

25. Teja, A.S.; Koh, P.-Y. Synthesis, properties, and applications of magnetic iron oxide nanoparticles. *Prog. Cryst. Growth Charact. Mater.* **2009**, *55*, 22–45. [CrossRef]

26. Ivantsov, R.; Evsevskaya, N.; Saikova, S.; Linok, E.; Yurkin, G.; Edelman, I. Synthesis and characterization of $Dy_3Fe_5O_{12}$ nanoparticles fabricated with the anion resin exchange precipitation method. *Mater. Sci. Eng. B* **2017**, *226*, 171–176. [CrossRef]

27. Saikova, S.V.; Trofimova, T.V.; Pavlikov, A.Y.; Samoilo, A.S. Effect of Polysaccharide Additions on the Anion-Exchange Deposition of Cobalt Ferrite Nanoparticles. *Russ. J. Inorg. Chem.* **2020**, *65*, 291–298. [CrossRef]

28. Trofimova, T.V.; Saikova, S.V.; Panteleeva, M.V.; Pashkov, G.L.; Bondarenko, G.N. Anion-Exchange Synthesis of Copper Ferrite Powders. *Glass Ceram.* **2018**, *75*, 74–79. [CrossRef]

29. Enache, T.A.; Oliveira-Brett, A.M. Peptide methionine sulfoxide reductase A (MsrA): Direct electrochemical oxidation on carbon electrodes. *Bioelectrochem* **2013**, *89*, 11–18. [CrossRef]

30. Khoury, R.A.; Ranasinghe, J.C.; Dikkumbura, A.S.; Hamal, P.; Kumal, R.R.; Karam, T.E.; Smith, H.T.; Haber, L.H. Monitoring the Seed-Mediated Growth of Gold Nanoparticles Using in Situ Second Harmonic Generation and Extinction Spectroscopy. *J. Phys. Chem.* **2018**, *122*, 24400–24406. [CrossRef]

31. Levin, C.S.; Hofiman, C.; Ali, T.A.; Kelly, A.T.; Morosan, E.; Nordlander, P.; Whitmire, K.H.; Halas, N.J. Magnetic-Plasmonic Core-Shell Nanoparticles. *ACS Nano.* **2009**, *3*, 1379–1388. [CrossRef] [PubMed]

32. Kim, G.; Weiss, S.; Levine, R. Methionine Oxidation and Reduction in Proteins. *Biochim. Biophys. Acta* **2014**, *1840*, 901–905. [CrossRef] [PubMed]

33. Glišić, B.; Djuran, M.; Stanić, Z.; Rajković, S. Oxidation of methionine residue in Gly-Met dipeptide induced by [Au(en)Cl$_2$]$^+$ and influence ofthe chelated ligand on the rate of this redox process. *Gold Bull.* **2014**, *47*, 33–40. [CrossRef]

34. Angelova, P.; Solel, E.; Parvari, G.; Turchanin, A.; Botoshansky, M.; Gölzhäuser, A.; Keinan, E. Chemisorbed Monolayers of Corannulene Penta-Thioethers on Gold. *Langmuir* **2013**, *29*, 2217–2223. [CrossRef]

35. Chen, K.; Li, H.J.W.; Xu, Y.; Liu, K.; Li, H.; Xu, X.; Qiu, X.; Liu, M. Untying Thioether Bond Structure Enabled by "Voltage-Scissors" for Stable Room Temperature Sodium-Sulfur Batteries. *Nanoscale* **2019**, *11*, 5967–5973. [CrossRef]

36. Bergès, J.; de Oliveira, P.; Fourré, I.; Houée-Levin, C. The One-Electron Reduction Potential of Methionine-Containing Peptides Depends on the Sequence. *J. Phys. Chem. B* **2012**, *116*, 9352–9362. [CrossRef]

37. Mikhlin, Y.L.; Nasluzov, V.A.; Romanchenko, A.S.; Shor, A.M.; Pal'yanova, G.A. XPS and DFT studies of the electronic structures of AgAuS and Ag_3AuS_2. *J. Alloys Compd.* **2014**, *617*, 314–321. [CrossRef]

38. Palyanova, G.; Mikhlin, Y.; Zinina, V.; Kokh, K.; Seryotkin, Y.; Zhuravkova, T. New gold chalcogenides in the Au-Te-Se-S system. *J. Phys. Chem. Solids.* **2020**, *136*, 109276. [CrossRef]

39. Radnik, J.; Mohr, C.; Claus, P. On the origin of binding energy shifts of core levels of supported gold nanoparticles and dependence of pretreatment and material synthesis. *Phys. Chem. Chem. Phys.* **2003**, *5*, 172–177. [CrossRef]

40. Arrii, S.; Morfin, F.; Renouprez, A.J.; Rousset, J.L. Oxidation of CO on Gold Supported Catalysts Prepared by Laser Vaporization: Direct Evidence of Support Contribution. *J. Am. Chem. Soc.* **2004**, *126*, 1199–1205. [CrossRef]

41. Kruse, N.; Chenakin, S. XPS characterization of Au/TiO2 catalysts: Binding energy assessment and irradiation effects. *Appl. Catal. A* **2011**, *391*, 367–376. [CrossRef]

42. Li, P.; Ma, R.; Zhou, Y.; Chen, Y.; Liu, Q.; Peng, G.; Liang, Z.; Wang, J. Spinel nickel ferrite nanoparticles strongly cross-linked with multiwalled carbon nanotubes as a bi-efficient electrocatalyst for oxygen reduction and oxygen evolution. *RSC Adv.* **2015**, *5*, 73834–73841. [CrossRef]

43. Zvezdin, A.K.; Kotov, V.A. *Modern Magnetooptics and Magnetooptical Materials*; IOP Publishing: Bristol, UK; Philadelphia, PA, USA, 1997; p. 404.

44. Himcinschi, C.; Vrejolu, I.; Salvan, G.; Fronk, M.; Talkenberger, A.; Zahn, D.; Rafaja, D.; Kortus, J. Optical and magneto-optical study of nickel and cobalt ferrite epitaxial thin films and submicron structures. *J. Appl. Phys.* **2013**, *113*, 084101. [CrossRef]

45. Verde, E.; Landi, G.; Carriao, M.; Drummond, I.; Gomes, J.; Vieira, E.; Sousa, M.; Bakuzis, A. Field dependent transition to the non-linear regime in magnetic hyperthermia experiments: Comparison between maghemite, copper, zinc, nickel and cobalt ferrite nanoparticles of similar sizes. *AIP Adv.* **2012**, *2*, 032120. [CrossRef]